ADVANCED MATERIALS
www.advmat.de

Microporogen-Structured Collagen Matrices for Embedded Bioprinting of Tumor Models for Immuno-Oncology

*Daniel S. Reynolds, Irene de Lázaro, Manon L. Blache, Yutong Liu, Nicholas C. Jeffreys, Ramsey M. Doolittle, Estée Grandidier, Jason Olszewski, Mason T. Dacus, David J. Mooney, and Jennifer A. Lewis**

Embedded bioprinting enables the rapid design and fabrication of complex tissues that recapitulate in vivo microenvironments. However, few biological matrices enable good print fidelity, while simultaneously facilitate cell viability, proliferation, and migration. Here, a new microporogen-structured (µPOROS) matrix for embedded bioprinting is introduced, in which matrix rheology, printing behavior, and porosity are tailored by adding sacrificial microparticles composed of a gelatin–chitosan complex to a prepolymer collagen solution. To demonstrate its utility, a 3D tumor model is created via embedded printing of a murine melanoma cell ink within the µPOROS collagen matrix at 4 °C. The collagen matrix is subsequently crosslinked around the microparticles upon warming to 21 °C, followed by their melting and removal at 37 °C. This process results in a µPOROS matrix with a fibrillar collagen type-I network akin to that observed in vivo. Printed tumor cells remain viable and proliferate, while antigen-specific cytotoxic T cells incorporated in the matrix migrate to the tumor site, where they induce cell death. The integration of the µPOROS matrix with embedded bioprinting opens new avenues for creating complex tissue microenvironments in vitro that may find widespread use in drug discovery, disease modeling, and tissue engineering for therapeutic use.

1. Introduction

Direct and embedded bioprinting methods offer tremendous potential for creating human tissue models for pharmaceutical and therapeutic applications.[1–7] One such application is immuno-oncology where organotypic tumor models are needed to improve the mechanistic understanding of immune-cell effects, develop new immunotherapies that promote effector cell-mediated anticancer responses, and predict patient-specific responses for personalized medicine.[8–12] It is essential that these models recapitulate the cellularly dense, heterogeneous structure of the in vivo tumor microenvironment, while simultaneously permitting immune-cell migration and function.[13] Although microfluidic-based tumor models have recently been developed, they often lack the ability to spatially pattern multiple cell types required to constitute the heterogeneous in vivo tumor microenvironment.[14–19] 3D tumor models have also been produced by direct bioprinting in a layer-wise manner, but these models are often limited by poor print resolution[20] or inadequate cell migration.[21,22] Such deficiencies stem from the use of extracellular matrices that hinder cell migration and function, because their viscoelasticity, biodegradability, and porosity differ substantially from in vivo microenvironments.[23,24] To improve encapsulated cell function, stiff bioinks with engineered microporosity arising from phase separation of two immiscible aqueous solutions[25–29] or microtemplated porogels[30] were recently introduced for direct bioprinting. By contrast, less attention has been devoted to the development of biological matrices for embedded printing.

Embedded bioprinting is an emerging method that requires both printable bioinks and viscoplastic matrices to facilitate nozzle translation and support patterning of high-fidelity features.[31,32] To date, hydrogel matrices composed of jammed microgel particles (≈100–1000 µm in diameter) have been generated with desirable properties for embedded bioprinting.[33–40] However, they possess a stiffness that is often orders of magnitude higher than native human tissues coupled with an intraparticle mesh size (≈10–100 nm) that is far below that of

D. S. Reynolds, I. de Lázaro[+], M. L. Blache, Y. Liu, N. C. Jeffreys, R. M. Doolittle, E. Grandidier, J. Olszewski, M. T. Dacus, D. J. Mooney, J. A. Lewis
John A. Paulson School of Engineering and Applied Sciences and the Wyss Institute for Biologically Inspired Engineering
Harvard University
Cambridge, MA 02138, USA
E-mail: jalewis@seas.harvard.edu

M. L. Blache, E. Grandidier
École Polytechnique Fédérale de Lausanne
Lausanne 1015, Switzerland

E. Grandidier
École Normale Supérieure de Lyon
Lyon 69007, France

J. Olszewski
Department of Bioengineering
Northeastern University
Boston, MA 02115, USA

The ORCID identification number(s) for the author(s) of this article can be found under https://doi.org/10.1002/adma.202210748

[+]Present address: Biomedical Engineering Department, New York University, New York City, NY 10003, USA

DOI: 10.1002/adma.202210748

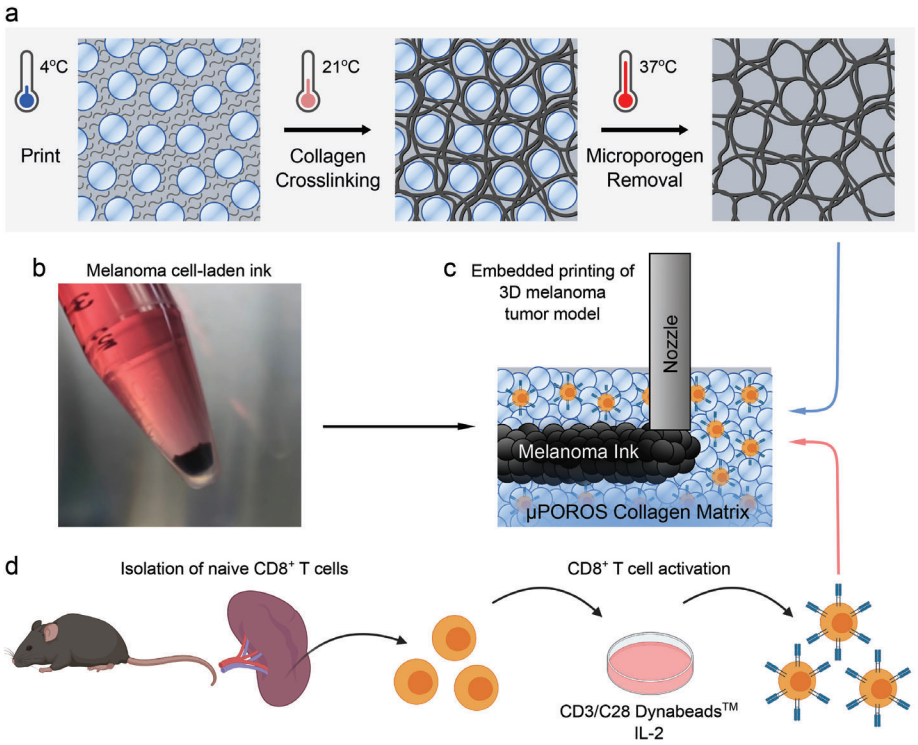

Figure 1. Creating microporogen-structured (μPOROS) collagen matrices for embedded bioprinting of 3D tumor models. a) At 4 °C, the sacrificial microparticles (MPs) (blue) serve as rheology modifiers that enable embedded bioprinting of cell-laden inks. At 21 °C, collagen matrix undergoes crosslinking (gray). At 37 °C the MPs melt and are washed away leaving behind a microporous collagen matrix. b,c) A melanoma cell-laden ink (black) with a cell density of 250 million cells mL^{-1} is patterned within the μPOROS collagen matrix at 4 °C via embedded bioprinting. d) T-cell-mediated tumor killing is demonstrated within the model via isolation of naïve, antigen-specific $CD8^+$ T cells from mice, activation with CD3/CD28 Dynabeads and IL-2, and incorporation into the μPOROS collagen matrix. c,d) Created using Biorender.com.

individual cells (≈10 μm). Consequently, cells spread and migrate along the microgel particle surfaces and interstices rather than within a 3D physiologically relevant environment. When the microgel particle size is on the order of the cell size, e.g., for Carbopol microgels,[41–43] the 3D cell morphology and printing resolution are improved. However, these synthetic microgels are not biodegradable and scatter light making live-cell imaging difficult. To circumvent challenges associated with jammed granular matrices, recent approaches have leveraged the sol–gel transition of native extracellular matrix-derived (ECM) matrices, such as Matrigel/collagen mixtures[44] or decellularized porcine skin.[45] While these native ECM-derived matrices possess inherent bioactivity, they suffer from extremely short print windows (<3 min) and poor print fidelity due to gravity-induced sedimentation. Hence, despite these promising advances, bioinks and matrices that better recapitulate the in vivo 3D microenvironment are needed for bioprinting.

Here, we report a new microporogen-structured (μPOROS) matrix for embedded bioprinting of tumor models for immuno-oncology. Our μPOROS matrix contains sacrificial microparticles that simultaneously serve as rheology modifiers to improve printability and microporogens to generate an interconnected microporous network that is permissive to key cellular processes (**Figure 1**). While our approach is broadly applicable, we focused on collagen type-I, the most abundant extracellular matrix protein in vivo,[46] which is often overexpressed in solid tumors.[47–49] However this biological matrix lacks the desired shear-thinning and yield stress properties required for embedded bioprinting.[50] To overcome this limitation, we incorporated sacrificial gelatin–chitosan microparticles of varying size and concentration within a prepolymer collagen solution to tailor their rheological properties for embedded printing at 4 °C (Figure 1a). Upon raising the temperature to 21 °C, the collagen crosslinks around sacrificial microparticles (Figure 1a). Upon further increasing the temperature to 37 °C, the sacrificial microparticles melt providing interconnected microporosity (Figure 1a). Importantly, our approach gives rise to a fibrillar network akin to that observed for in vivo collagen type-I.[46] As an exemplar, we produced a murine melanoma model with physiologically-relevant cell densities[51,52] (≈250 million cells mL^{-1}) and clinically relevant tumor diameters[53] (0.5–1.5 mm) by printing a murine melanoma cell ink within our μPOROS collagen matrix (Figure 1b). Finally, to demonstrate the functionality of our 3D tumor model, we show that antigen-specific cytotoxic T cells can migrate through the μPOROS matrix and initiate cancer cell killing, thereby reducing the tumor volume (Figure 1c,d).

2. Results and Discussion

We first generated sacrificial microparticles composed of gelatin type A and chitosan by modifying a previously reported method for complex coacervation.[6] Suitable microparticles must meet

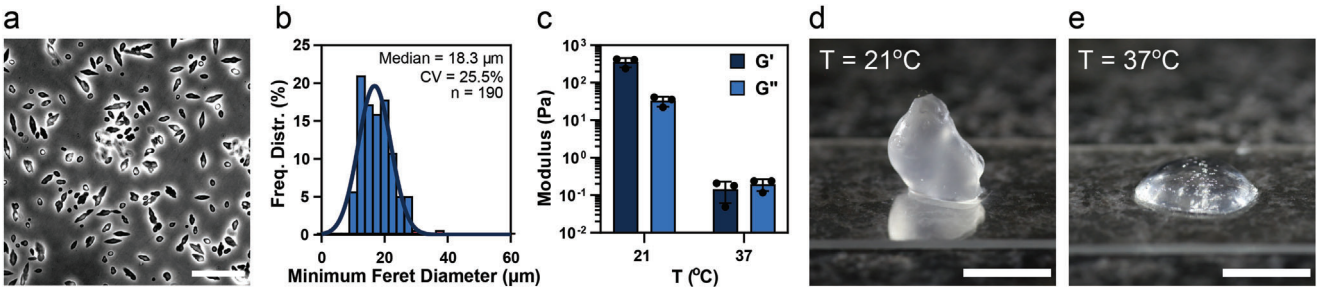

Figure 2. Generating sacrificial microparticles. a) Bright-field image of sacrificial microparticles (MPs) composed of gelatin Type A and chitosan. Scale bar = 100 µm. b) MP size distribution. c) Semilog plot of the storage (G') and loss (G'') moduli as a function of temperature for a compacted MP slurry; data are presented as mean ± SD, n = 3. d,e) Representative images of this MP slurry, which highlight the solid-to-fluid phase transition that occurs upon warming from 21 to 37 °C. Scale bar = 10 mm.

several criteria: 1) possess a characteristic size on the order of individual cells to facilitate cell migration,[54] 2) serve as a rheology modifier for embedded bioprinting, and 3) exhibit the appropriate phase behavior to enable their removal from the matrix under physiological conditions. We systematically varied the microparticle size between 6 and 120 µm by tuning the gelatin bloom strength and ethanol concentration (Figures S1 and S2, Supporting Information). When a high bloom strength (250 g) and 51.5 (v/v)% ethanol are used, gelatin–chitosan microparticles are produced with a characteristic size of ≈18 µm (**Figure 2**a,b), akin to the size of individual cells and above the ≈2–3 µm pore size previously shown to restrict cell migration via mechanical confinement.[54] Upon suspending and consolidating these microparticles into a jammed state, the system behaves like a viscoplastic gel at 21 °C with a storage modulus, G', of ≈350 Pa that exceeds the loss modulus, G'' (Figure 2c). When warmed to 37 °C, the jammed microparticles undergo a gel-to-liquid transition resulting in a G' value of ≈0.2 Pa accompanied by a pronounced shape change (Figure 2d,e). This phase transition occurs in roughly 45 min, i.e., the time required to reach the $G'' > G'$ crossover (Figure S3, Supporting Information).

Next, we created µPOROS matrices by incorporating the sacrificial microparticles within a prepolymer solution containing 4 mg mL^{-1} of collagen type-I at 4 °C. Absent microparticles, the pure collagen solution is a viscous liquid with a low shear viscosity of ≈3 Pa s, which does not exhibit a shear yield stress (**Figure 3**a,b) and therefore is unsuitable for embedded printing. At a microparticle volume fraction (ϕ) of 0.47, the resulting µPOROS matrix exhibits a low shear viscosity of ≈30 000 Pa s and a shear yield stress (τ_y) of ≈20 Pa. Importantly, these values, which are roughly three orders of magnitude higher than those measured for the pure prepolymer solution, are sufficient for embedded printing.[1,4,32] At 4 °C, this matrix (microparticle ϕ = 0.47) exhibits a solid-like response ($G' > G''$) when the applied shear stress, $\tau < \tau_y$ (Figure 3c). When warmed to 21 °C, collagen crosslinks around the sacrificial microparticles, which remain in a gelled state. This transition is accompanied by a pronounced increase in G' from ≈230 Pa at 4 °C to ≈470 Pa at 21 °C. As the temperature is further increased to 37 °C, the microparticles melt resulting in a softer collagen matrix ($G' \approx 110$ Pa) that remains in a solid-like state even after microparticle removal. Individual microparticles are readily visualized by incorporating a high MW fluorescein isothiocyanate (FITC)–dextran in the prepolymer solution (Figure 3d) and their ϕ can be tailored between 0.20 and 0.60 (Figure S4, Supporting Information) by varying the centrifugation speed used during consolidation. It is therefore possible to independently control the characteristic pore size and total porosity of these µPOROS matrices (Figure S5, Supporting Information). Indeed, confocal laser scanning reflectance microscopy confirms the presence of a stable collagen network that consists of a fibrillar structure, akin to collagen type-I in vivo (Figure 3e) with a median pore size ≈12 µm (Figure S5, Supporting Information). Moreover, the µPOROS collagen material properties can be further tuned by changing the collagen concentration, microparticle ϕ and diameter (d). For example, after removal of the microparticles, G' is higher for matrices with higher collagen concentration (Figure S6, Supporting Information) at a constant microparticle ϕ and d. While varying the microparticle ϕ from ≈0.4–0.5 (d = 18 µm) by centrifuging the matrices from 1000g to 3000g, respectively, results in an eightfold increase in τ_y from ≈4 to ≈32 Pa, while G' remains roughly 100 Pa after microparticle removal (Figure S7, Supporting Information). We note that matrices composed of a fixed microparticle ϕ and varying d (from 6 to 43 µm) also had a similar G' values after microparticle removal (Figure S8, Supporting Information). Finally, we carried out a removal assay using fluorescein-conjugated microparticles to demonstrate that the gelatin microparticles are almost fully removed from these matrices within 5 days (Figure S9, Supporting Information).

To integrate µPOROS matrices with embedded bioprinting, we created a bioink composed of murine melanoma cells (B16-F10) at a concentration of ≈250 million cells mL^{-1}, a relevant value for in vivo tumor cell densities.[51,52] Next, this melanoma bioink is patterned in controlled tumor geometries via embedded printing within both µPOROS and pure collagen (control) matrices. As a representative example, we successfully printed a helical spiral with a 4 mm diameter and 2 mm pitch deep within our µPOROS collagen matrix with high feature fidelity (**Figure 4**a; Movie S1, Supporting Information). By contrast, when this same helical pattern is printed in the pure collagen matrix (control), it rapidly settles under gravity due to the significantly lower viscosity and negligible τ_y of this matrix (Figure 4a; Movie S1, Supporting Information). These differences in print fidelity are readily apparent after crosslinking both collagen-based matrices at 21 °C and subsequently removing the sacrificial microparticles at 37 °C (Figure 4b,c). We note that more complex geometries, such

as 1st and 2nd order Hilbert curves, can also be printed within our μPOROS matrix (Figure 4d,e). The diameter of printed filamentary features can be readily tuned by varying the print speed to create a range of clinically relevant tumor filament diameters (Figure S10, Supporting Information).[53] Actin staining on Day 0 and Day 7 shows that embedded B16-F10 melanoma tumor filaments remain stable (Figure 4f,g), while confocal reflectance microscopy reveals that these printed filaments are embedded in a fibrillar collagen matrix (Figure 4h,i). Finally, immunofluorescent staining for the proliferation marker, Ki67, reveals that B16-F10 cells both spread and proliferate within the μPOROS matrix (Figures S11 and S12, Supporting Information).

As a final demonstration, we created a 3D tumor model that recapitulates antitumor immunity by incorporating antigen-specific, cytotoxic T cells within our μPOROS collagen matrix (Figure 1c,d). Using this model, we assess cytotoxic T cell migration, infiltration, and antitumor activity within our μPOROS collagen matrix. We first isolated antigen-specific CD8$^+$ T cells from the spleen of pmel-1 mice. These T cells, which recognize the pmel-17 antigen (a mouse homologue of human gp100) on B16-F10 melanoma cells, have previously been shown to significantly slow tumor progression in an established murine tumor model.[55] Since T cell migration is critical to the underlying biology of antitumor immunity in vivo,[13] we first carried out a migration assay of pmel-1 CD8$^+$ T cells encapsulated within printable μPOROS collagen matrices. As controls, we investigated T cell migration within both methacrylated gelatin (GelMA), a commonly used bioink, and pure collagen matrices. On Day 1, the mean migration speed of pmel-1 CD8$^+$ T cells is 0.82 ± 0.26, 0.02 ± 0.003, 0.03 ± 0.002, 1.40 ± 0.26, and 0.67 ± 0.01 μm min^{-1} for μPOROS collagen, 5 wt% GelMA, 10 wt% GelMA, 2 mg mL^{-1} pure collagen, and 4 mg mL^{-1} pure collagen, respectively (**Figure 5**a). By Day 3, mean migration speed of these cells increased to 1.54 ± 0.24, 3.01 ± 0.23, and 2.10 ± 0.26, μm min^{-1} for μPOROS collagen, 2 mg mL^{-1} pure collagen, and 4 mg mL^{-1} pure collagen matrices, respectively (Figure 5a). Importantly, the migration speed of these pmel-1 CD8$^+$ T cells in our μPOROS collagen matrix is roughly 30–40 times higher than that observed for printable GelMA matrices (due to their high confinement) and comparable to that observed in pure collagen, which is not suitable for embedded bioprinting. Importantly, the observed migration speed of these T cells within our μPOROS collagen matrix is akin to values reported for their in vivo migration.[56–59] Our analysis of pmel-1 CD8$^+$ T cell migration is shown in Figure S13 of the Supporting Information, which is based on direct visualization (Movies S2–S6, Supporting Information). We note that T cell viability in our μPOROS collagen matrix is nearly identical to pure collagen matrices (Figure 5b).

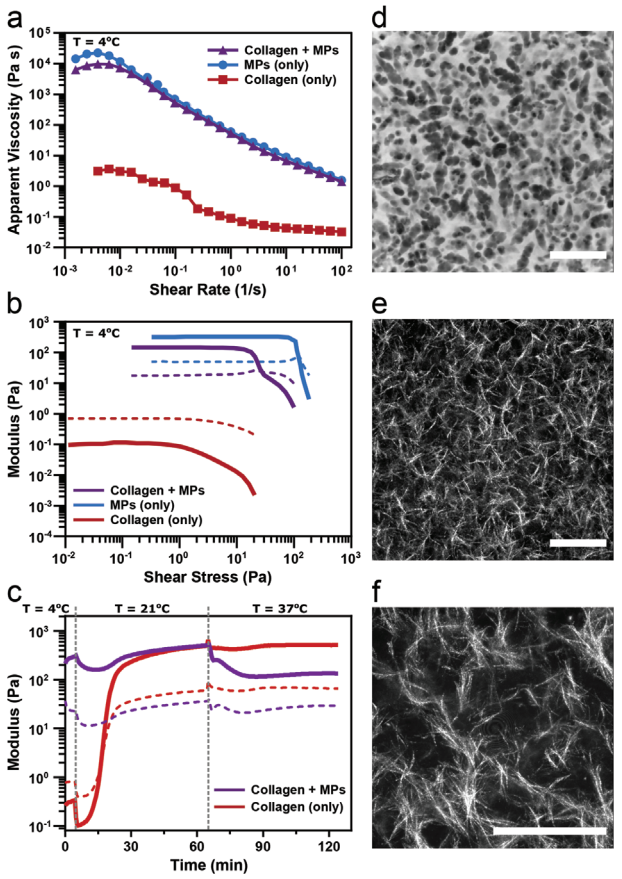

Figure 3. μPOROS collagen matrices. a) Log–log plot of apparent viscosity as a function of shear rate for a pure 4 mg mL^{-1} collagen matrix (red), pure MP slurry (light blue), and MP-laden (μPOROS) 4 mg mL^{-1} collagen matrix (purple) at $T = 4$ °C. b) Log–log plot of shear storage modulus (G') (continuous line) and loss modulus (G'') (dotted line) as a function of shear stress at $T = 4$ °C. c) Semilog plot of G' (continuous line) and G'' (dotted line) as a function of temperature and time representative of printing workflow. d) Representative optical image of MPs ($\phi = 0.47$) encapsulated within a collagen matrix. e,f) Representative confocal reflectance images of μPOROS collagen matrix at 37 °C following MP removal. Sale bar = 100 μm.

Next, we patterned B16-F10 melanoma tumor filaments within a μPOROS collagen matrix that contained pmel-1 CD8$^+$ T cells via embedded printing. As a control, we also printed samples with CD8$^+$ T cells isolated from the spleen of wild-type C57BL/6J mice that do not recognize the pmel-17 antigen on B16-F10 melanoma cells. Each tumor filament is printed within 500 μL of μPOROS collagen matrix that contains CD8$^+$ T cells seeded at 4 × 10^6 cells mL^{-1} at an effector:tumor cell ratio of ≈5.4, which has previously been shown to promote T-cell-mediated tumor cell killing in nonadherent and 2D culture in vitro systems.[60–63] The printed B16-F10 melanoma filaments are 660 ± 27 μm in diameter and 4.6 ± 0.2 mm in length on Day 0 (Figure S14, Supporting Information) with an initial cell density of 2.37 ± 0.18 × 10^8 cells mL^{-1}. In the control containing wild-type CD8$^+$ T cells, the printed tumor diameter increases by a factor of two over a 21-day culture period (Figure S15, Supporting Information). Fluorescent labeling of the cells with independent CellTracker stains followed by imaging on Day 0 confirmed the presence of CD8$^+$ T cells in the μPOROS collagen matrices surrounding the embedded melanoma tumor filaments (Figure S16, Supporting Information). Time-lapse imaging revealed pmel-1 CD8$^+$ T cells migrate and begin infiltrating the printed B16-F10 melanoma filament within 6 h after printing (Movie S7, Supporting Information). Longitudinal analysis of the tumor volume via actin staining showed that the addition of pmel-1 CD8$^+$ T cells led to a statistically significant reduction by Day 3 compared to the control tumors with and without wild-type CD8$^+$ T cells (Figure 5c). On Day 6, the normalized tumor volume increased

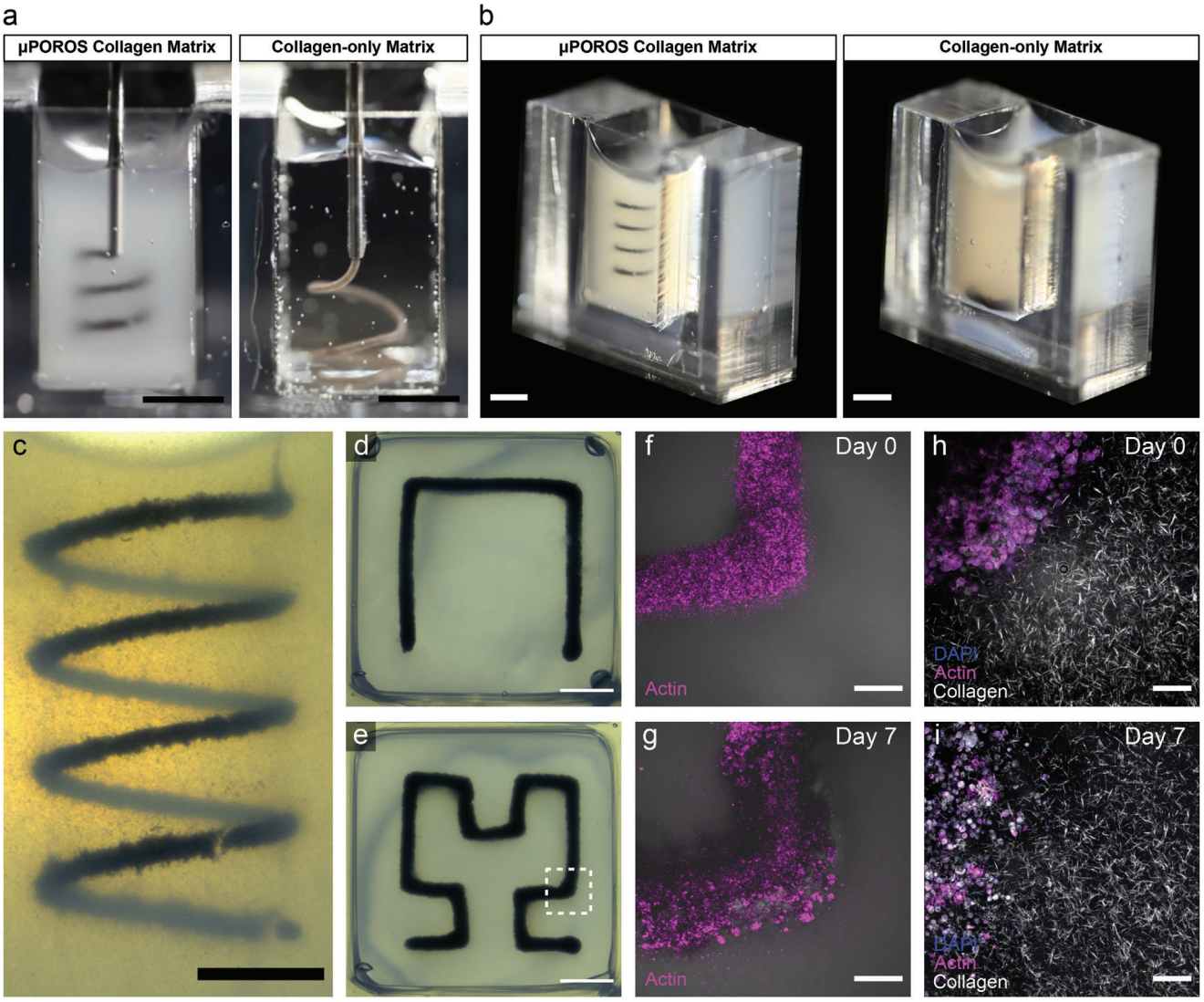

Figure 4. 3D melanoma tumor model printed within μPOROS collagen matrix. a) A B16-F10 murine melanoma cell ink (≈2.5 × 10^8 cells mL^{-1}) is deposited within a μPOROS collagen or pure collagen-only (control) matrix at 4 °C. Scale bar = 4 mm. b) Printed melanoma tumor filaments embedded within this μPOROS collagen matrix following crosslinking at 21 °C and MP removal at 37 °C, respectively. Scale bar = 4 mm. c) Side view of printed helix with 4 mm diameter and 2 mm pitch embedded within this μPOROS collagen matrix. Scale bar = 2 mm. d,e) Bottom view of melanoma tumor filaments deposited as a first-order Hilbert curve (d) and a second-order Hilbert curve (e). Scale bar = 2 mm. f,g) Actin stain of deposited melanoma filament within μPOROS collagen matrix on Day 0 (f) and Day 7 (g). Scale bar = 500 μm. h,i) Confocal reflectance imaging reveals the melanoma tumor filament is deposited within fibrillar μPOROS collagen matrices. (f)–(i) correspond to the boxed area in (e). Scale bar = 100 μm.

by a factor of 1.6 ± 0.25 and 1.1 ± 0.16 for controls without and with wild-type $CD8^+$ T cells, respectively. By contrast, tumors embedded within a μPOROS collagen matrix that contained pmel-1 $CD8^+$ T cells decreased by nearly threefold in volume over the same time period.

To further assess their antitumor response, we performed a viability assay on printed tumors in *μ*POROS matrices containing pmel-1 $CD8^+$ T cells on Day 3 and Day 6 using acridine orange (AO) and propidium iodide (PI). We first observed an elevated expression of granzyme B, interferon gamma, and tumor necrosis factor alpha in the culture media revealing pmel-1 $CD8^+$ T cells activation, which is not observed in our control tumors with or without wild-type $CD8^+$ T cells (Figure S17, Supporting Information). These cytotoxic pmel-1 $CD8^+$ T cells give rise to elevated tumor cell death with a measured cell viability of 69.2% ± 13.2% on Day 3 and 14.6% ± 5.9% on Day 6 (Figure 5d; Figure S18, Supporting Information). By contrast, the control tumors with and without wild-type $CD8^+$ T cells exhibited high cell viability >90% at both time points. Representative images from the AOPI viability assay at the mid-plane of the filaments are shown in Figure 5e. The striking difference in tumor cell viability in the presence of wild-type vs pmel-1 $CD8^+$ T cells indicates that the antitumor immunity is antigen-specific, i.e., only pmel-1 $CD8^+$ T cells are capable of recognizing the pmel-17 antigen on B16-F10 melanoma cells to induce cell killing. The viability assay performed on Day 3 further reveals that cell death originates at the outer periphery

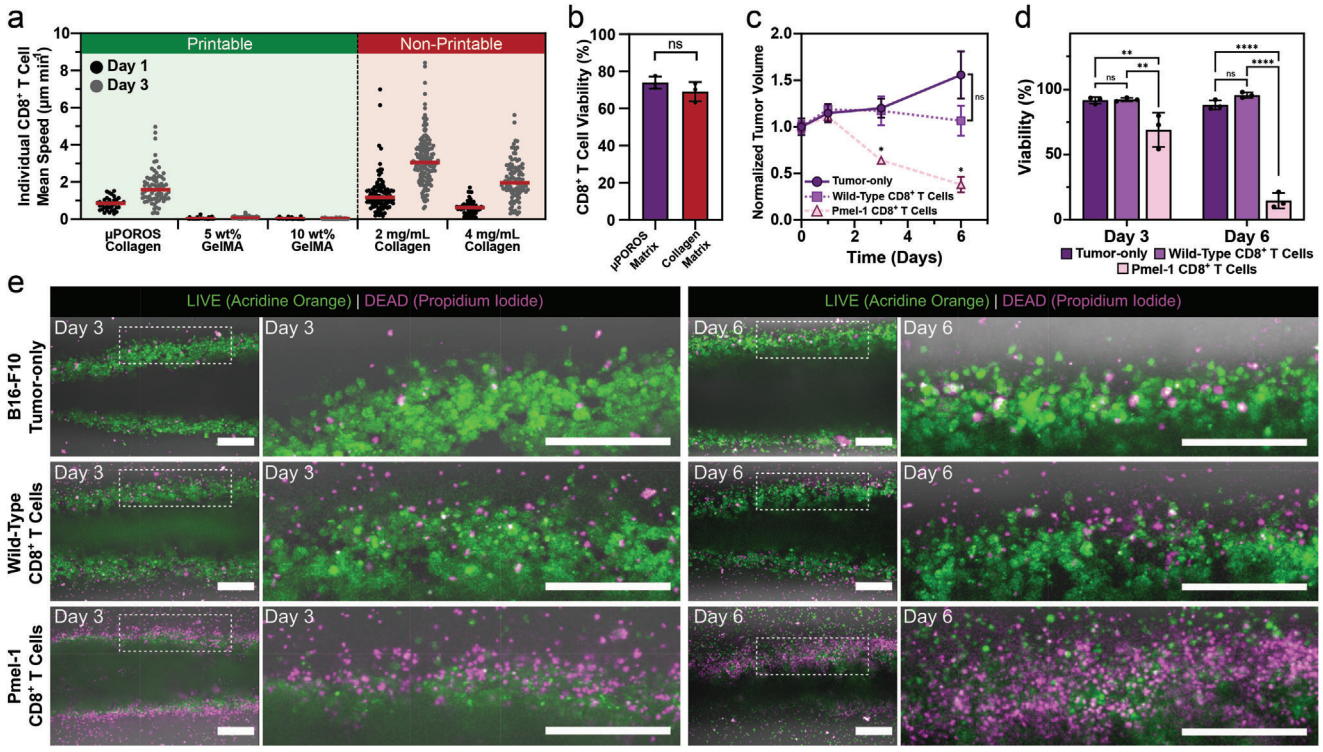

Figure 5. T-cell-mediated tumor killing within 3D melanoma tumor model. a) pmel-1 CD8$^+$ T cell migration assay on Day 1 and Day 3. Red line represents median individual cell speed ($n = 4$ biological replicates) observed within different matrices, including μPOROS collagen, methacrylated gelatin (GelMA), and pure collagen (controls). b) Cell viability analysis of pmel-1 CD8$^+$ T cells in both μPOROS and pure (control) collagen matrices. Data are presented as mean ± SD, $n = 3$. c) Longitudinal assay of melanoma tumor volume without immune cells (circle, control), with wild-type CD8$^+$ T cells (square, control), and with pmel-1 CD8$^+$ T cells (triangle) incorporated within the μPOROS collagen matrices. Data are presented as mean ± SD, $n = 3$, p-values are calculated using two-way ANOVA with Holm–Sidak correction (* $p < 0.05$, $n = 3$). d) Cell viability analysis on Day 3 and Day 6 for the same models. Data are presented as mean ± SD, $n = 3$, p-values are calculated using two-way ANOVA with Holm–Sidak correction (** $p < 0.01$, **** $p < 0.0001$). e) Representative cell viability images taken on Day 3 and Day 6 at the mid-plane of each printed melanoma tumor without immune cells (circle, control), with wild-type CD8$^+$ T cells (square, control), and with pmel-1 CD8$^+$ T cells (triangle) incorporated within the μPOROS collagen matrices. Scale bar = 250 μm.

of the printed tumor, likely due to T cell migration from the surrounding μPOROS collagen matrix followed by their subsequent infiltration into the printed tumors. Finally, we find that the tumor structure breaks down over time on in the presence of pmel-1 CD8$^+$ T cells (Movie S8, Supporting Information).

3. Conclusion

We have created a new class of printable, microporous biological matrices for embedded printing. By using sacrificial microparticles as both rheology modifiers and microporogens, we have achieved high fidelity printing of tumor models within a porous microenvironment that facilitates cell spreading, proliferation, and migration. While this approach is generalizable to other matrices, we focused our efforts on creating μPOROS collagen type-I matrices that enable tumor cell patterning, proliferation, and migration within a microporous matrix that exhibits a fibrillar structure akin to in vivo matrices. We used embedded printing in μPOROS matrices to generate 3D melanoma tumor models for immuno-oncology applications with high cellular density and immune-cell–tumor interactions akin to their in vivo counterparts. We showed that antigen-specific, cytotoxic T cells migrate to the tumor site, where they initiate antigen-specific cell killing. Looking ahead, we anticipate that μPOROS matrices coupled with embedded bioprinting may be widely adopted for creating human tissues for drug testing, disease modeling, and tissue engineering applications.

4. Experimental Section

Sacrificial Microparticles: The sacrificial microparticles were generated using a coacervation method modified from the literature.[6] First, 2.0% (w/v) gelatin Type A (Sigma-Aldrich), 0.25% (w/v) Pluronic F-127 (Sigma-Aldrich), and 0.1% (w/v) chitosan (Sigma-Aldrich) were dissolved in 51.5% (v/v) ethanol solution with stirring at 45 °C and pH adjusted to 6.32 by addition of 1 N sodium hydroxide (NaOH). Microparticles were formed by removing the solution from heat and allowing the solution to reach room temperature with stirring overnight. To isolate the microparticles, the microparticle slurry was divided into 50 mL conical tubes and spun at 2000g. The supernatant was removed, and the resulting microparticle pellets were mechanically homogenized using a gentleMACS dissociator (Miltenyi Biotec) and resuspended in 1× PBS. The microparticles were then washed three additional times via centrifugation at 2000g, removal of supernatant, mechanical dissociation of the pellet by manual pipetting, and resuspension in 1× PBS. Microparticles were stored in

1× PBS at 4 °C and used within 6 months. The size and distribution of microparticles were measured by bright-field imaging and analyzed using a custom-written ImageJ script. A suspension of microparticles in 1× PBS were placed in a 6-well plate and imaged after microparticles settled to the bottom of the well.

To characterize their rheological and melting behavior, a slurry of sacrificial microparticles was deposited onto the rheometer and their storage (G') and loss (G'') moduli were measured at 21 °C before immediately raising to 37 °C. Measurements were taken every 30 s for 1 h to record melting kinetics. Next, a temperature sweep was carried out to characterize the microparticle melting temperature. Their G' and G'' values were recorded between 20 and 40 °C in 1 °C increments with 30 min dwell time between each step. To characterize the gelation and melting kinetics of the μPOROS collagen matrix, an oscillatory strain of 1% and frequency of 1 Hz was applied for 5 min at 4 °C, then 90 min at 21 °C, and finally 60 min at 37 °C.

μPOROS Collagen Matrices: Sacrificial microparticles were passed through a 40 μm cell filter (Corning Inc.) prior to each experiment. A 4 mg mL^{-1} collagen solution was created as previously described.[64–66] Briefly, high-concentration rat tail type I collagen (Corning Inc.) was combined 1:1 (v/v) with collagen neutralizing buffer (100 mM HEPES in 2× PBS, pH 7.8) and diluted to appropriate working concentration in 1× PBS. The filtered microparticles were then suspended within 4 mg mL^{-1} collagen at a 1:1 (v/v) and centrifuged at 2000*g* for 5 min at 4 °C. The excess collagen was removed and 4 mg mL^{-1} collagen at a 2:1 (v/v) was added and subsequently centrifuged at 2000*g* for 5 min at 4 °C. The collagen/microparticle matrix was then kept on ice until printing. Printing typically occurred within 45 min after mixing of the microparticles and collagen, but the collagen/microparticle matrix could be kept on ice for 4 h and remained printable.

Matrix Characterization: Rheological measurements were carried out on μPOROS collagen matrices compacted within a 10 mL syringe via centrifugation. Excess collagen was removed and the remaining μPOROS collagen matrix was deposited onto the Peltier plate of a Discovery HR-3 stress-controlled rheometer (TA Instruments). A 25 mm diameter geometry was used and both the geometry and Peltier plate were coated with sandpaper to prevent slip and precooled to 4 °C. The gap height was brought to 1 mm and excess material was removed with a spatula. Apparent viscosities were measured by performing flow sweeps with shear rates between 0.001 to 100 s^{-1}. Shear yield stresses were measured by carrying out amplitude sweeps at 1 Hz with strains ranging between 1×10^{-3} and 1×10^{1}.

To determine their microparticle volume fraction, μPOROS collagen matrices were produced with 2 MDa FITC–dextran (Sigma-Aldrich) at 5% (w/v) added to the collagen prepolymer solution at 4 °C following a protocol adapted from the literature.[39] The μPOROS collagen matrix was prepared in 5 mL Eppendorf tubes and then transferred to a custom chamber via a 1 mL syringe (Becton Dickenson Co.) with a tapered 1.6 mm inner-diameter nozzle (Nordson EFD). The custom chambers were made from 8 mm-thick, laser-cut acrylic (McMaster-Carr) and 18 mm × 18 mm cover glass (Corning Inc.) adhered together by SE1700 silicone (Dow Corning). The samples were then imaged using an upright confocal microscope (LSM710, Zeiss) and analyzed via a custom MATLAB routine. To account for light scattering over the *Z*-stacks, contrast was enhanced in every image by saturating the lowest (<1%) and highest (>99%) pixel values. The area fraction was calculated based on the binary image created by using a threshold fixed at 50% of the maximum pixel intensity. The microparticle volume fraction was computed as the mean area fraction over all *Z*-stack images in the sample.

The resulting pore size and distribution within the μPOROS collagen matrices were determined after removing microparticles of different size (6–42 μm in diameter) by carrying out confocal imaging and image analysis using Imaris (Bitplane Inc.). Confocal *Z*-stacks of the μPOROS collagen matrices were first inverted. Spot objects were then added to identify and measure the size of each pore. Using the algorithm setting "different spot sizes", the spots were selected for regional growth into spherical objects and then object–object statistics were used. The spherical objects were filtered and selected based on quality thresholds. Next, their diameters were measured and correlated to determine the median pore size of each μPOROS collagen matrix.

Microparticle Removal Kinetics: Fluorescein-conjugated gelatin was synthesized using NHS-Fluorescein (Thermo Fisher Scientific), as previously described in the literature.[29] The lyophilized fluorescein-conjugated gelatin was added 1:10 wt/wt to unlabeled gelatin during the fabrication of sacrificial microparticles as previously described. Fluorescein-conjugated microparticles were stored in 1× PBS at 4 °C in the dark until use. μPOROS collagen matrices were prepared with fluorescein-conjugated microparticles and 400 μL of material was deposited into custom culture chambers (10 mm × 10 mm × 5 mm) and allowed to crosslink at 21 °C for 1 h. After crosslinking, 800 μL of 1× PBS was added to the chambers and moved to 37 °C. At given time intervals, 400 μL of supernatant was collected and replaced with 400 μL of 1× PBS. After the final collection, the μPOROS collagen matrices were enzymatically degraded with Collagenase IV (Gibco) to collect the remaining fluorescein-conjugated gelatin. The fluorescent intensity from the collected samples was obtained using a plate reader (excitation 485 nm, emission 528 nm, BioTek Synergy HT).

Mice: All animal procedures were conducted in accordance with the Harvard University Faculty of Arts and Sciences (FAS) Institutional Animal Care and Use Committee (IACUC) guidelines. B6.Cg-Thy1a/Cy Tg(TcraTcrb)8Rest/J (pmel-1) mice (Jackson #005023), which are genetically modified to express the T cell receptor specific for the pmel-17 antigen of B16-F10 mouse melanoma cells, were purchased from the Jackson Laboratory. C57BL/6J mice (Jackson #000664) were also purchased from the Jackson Laboratory and used as controls. Mice were left to acclimatize to the animal facilities for at least 1 week before any procedures were conducted, and they were maintained in a 12 h light/12 h dark cycle with water and food ad libitum. All mice utilized in these studies were used between 6 and 12 weeks of age.

Cell Culture: The murine melanoma cell line B16-F10 (ATCC) was cultured in DMEM media supplemented with 10% (v/v) heat inactivated fetal bovine serum (Gibco) and 1% (v/v) antibiotic–antimycotic (Gibco). All experiments were performed with B16-F10 cells at passage 12 or lower.

Pmel-1 CD8$^+$ T cells were isolated from the spleens of pmel-1 mice (#005023, Jackson Laboratory), and wild-type CD8$^+$ T cells were isolated from the spleens of C57BL/6J mice (#000664, Jackson Laboratory), as described above. In brief, spleens were retrieved after carbon dioxide euthanasia, mechanically disrupted into single cell suspensions and filtered through a 70 μm mesh, and red blood cells were lysed with Red Blood Cell Lysis Buffer (Biovision), following the manufacturer's instructions. CD8$^+$ T cells were then isolated by magnetic cell sorting using the CD8a$^+$ Cell Isolation Kit for mouse (Miltenyi) and LS separation columns (Miltenyi). Isolated CD8$^+$ T cells were cultured in T cell media consisting of RPMI media supplemented with 5% (v/v) heat inactivated fetal bovine serum (Gibco), 1% antibiotic–antimycotic (Gibco), 1 mM sodium pyruvate, 1× nonessential amino acids (Thermo Fisher Scientific), 0.05 mM β-Mercaptoethanol (Sigma-Aldrich), and 24 ng mL^{-1} murine IL-2 (Peprotech), and activated with CD3/CD28 Dynabeads for mouse (Gibco) following the manufacturer's instructions. All animal studies were carried out in the laboratory of DJM, in accordance with institutional guidelines approved by Harvard University's IACUC.

4.0.0.1. Culture Chambers: For experiments in which the melanoma cell inks were cultured longitudinally, customized silicone culture chambers were fabricated via direct ink writing (Figure S19, Supporting Information). First, a 10:1 mass ratio of SE1700 base:curing agent (Dow Corning) was mixed using a SpeedMixer (Flacktek Inc.) at 2500 rpm for 1 min. The mixed silicone was then loaded into a 30 cm^3 syringe (Nordson EFD) and centrifuged at 3000*g* for 5 min to remove entrapped air. A tapered nozzle with 0.84 mm inner diameter (Nordson EFD) was attached to the outlet of the syringe. The syringe was mounted onto a custom 3D printer, and the silicone ink was dispensed via pressure generated from an Ultimus V pressure controller (Nordson EFD) onto 25 mm × 75 mm glass slides (Corning Inc.). The printing chambers contained a lower chamber (10 mm × 10 mm × 5 mm) that could accommodate up to 500 μL of μPOROS collagen matrix material, and an upper chamber (15 mm × 15 mm × 5 mm) that could accommodate up to 1 mL of cell culture media. Prior to use, the silicone chambers were cured at 85 °C overnight,

autoclaved, and pretreated with poly(D-lysine) and glutaraldehyde as previously described.[67] Alternatively, for printing helical features composed of the melanoma ink, acrylic chambers were fabricated using a laser cutter (Epilog Laser). A 10 × 10 mm notch was cut into a 10 mm-thick piece of acrylic, and 18 mm × 18 mm glass coverslips (Corning Inc.) were mounted to the sides of the acrylic chambers using SE1700 silicone as a sealant. In this set of experiments, 800 µL of either µPOROS collagen or collagen-only (control) matrices were loaded into each chamber.

Embedded Bioprinting: The 3D chambers were prechilled to 4 °C, and µPOROS collagen matrices were prepared and manually deposited into the printing chambers using a 1 mL syringe (Becton Dickenson Co.) with a tapered nozzle (1.6 mm inner diameter, Nordson EFD). The chambers with material were kept at 4 °C until printing. Next, a melanoma ink was prepared by compacting a cell suspension of B16-F10 cells in cell culture medium within a 1 mL glass syringe (Hamilton Co.) via centrifugation at 300*g* for 5 min. The cell density of the resulting cell ink was calculated by counting the total number of cells in a syringe using a Countess II (Thermo Scientific) hemocytometer and recording the volume of the resulting pellet in the syringe. Excess cell culture media was removed from the syringe, and a straight stainless-steel nozzle with an inner diameter of 0.410 mm (Nordson EFD) was attached. The syringe was mounted to a custom Arduino-controlled syringe extruder attached to the 3D printer.[1]

The printing chambers with µPOROS collagen matrix were placed on the 3D printer, and the melanoma cell ink was extruded at volumetric flow rate set to 0.1 µL s^{-1} and was kept constant across all experiments. The print speed ranged between 0.05 and 2 mm s^{-1}, and was set depending on the desired filament diameter. After deposition of the melanoma cell ink within the µPOROS collagen matrix, the chambers were placed at 21 °C for 1 h to allow the collagen to crosslink. After 1 h at 21 °C, the chambers were placed in a 37 °C incubator for 30 min to initiate melting of the sacrificial microparticles. After 30 min at 37 °C, 1 mL of cell culture media was added to each chamber and the media was changed daily.

Photographs and videos of tumor model fabrication were acquired using a DSLR camera (Canon EOS, 5D Mark II; Canon). Printed melanoma filaments were imaged using a Keyence Zoom (VHX-2000; Keyence), an inverted microscope (DM IL LED, Lieca) with a CCD camera (DFC7000 T, Lieca), an upright confocal microscope (LSM710, Zeiss), and an automated environmentally controlled, fluorescence microscope (Celldiscoverer 7, Zeiss).

T Cell Migration in µPOROS Matrices: Freshly isolated T cells were cultured with CD3/CD28 Dynabeads (Gibco) in T cell media supplemented with 24 ng mL^{-1} murine IL-2 (Peprotech). The cultures were split in fresh media when cell density exceeded 2.5 × 10^6 cells mL^{-1}. On Day 5, Dynabeads were separated from the T cells using an MACS Manual Separator (Miltenyi Biotec). Prior to embedding within the µPOROS collagen matrix, T cells were fluorescently labeled with CellTracker Orange CMRA dye (ThermoFisher Scientific). Here, T cells were washed two times with PBS, resuspended in 5 µM CellTracker Orange CMRA dye in base RPMI media without serum, and incubated with the CellTracker dye for 30 min at 37 °C. Following incubation with CellTracker dye, the T cells were washed two additional times with PBS.

The fluorescently labeled T cells were then suspended within a 4 mg mL^{-1} collagen solution at a concentration of 5 × 10^6 cells per mL. This collagen solution was added to the µPOROS collagen matrix at 1:10 (v/v) to yield a µPOROS collagen matrix with T cells at a final concentration of 5 × 10^5 cells per mL. To ensure homogeneity, the T cell-laden collagen material was gently mixed with the µPOROS collagen material using a 1 mL syringe with a tapered nozzle having an inner-diameter of 1.6 mm being sure to avoid the introduction of air bubbles into the material. Once mixed, the µPOROS collagen matrix containing fluorescently labeled T cells was transferred to 24-well glass-bottom plates (Mattek Co.). The glass-bottom plates were pretreated with poly-D-lysine (Sigma-Aldrich) and glutaraldehyde (Sigma-Aldrich) according to a previously established method[67] to facilitate anchoring of the µPOROS collagen material to the glass substrate. Each well received 125 µL of µPOROS collagen matrix material. As controls, fluorescently labeled T cells were incorporated into 4 and 2 mg mL^{-1} collagen gels. For the gelatin-methacrylate control, fluorescently labeled T cells were incorporated into 5 and 10 wt% gelatin-methacrylate (PhotoGel, Advanced Biomatrix) with 2 mM lithium phenyl-2,4,6-trimethylbenzoylphosphinate (LAP) (Sigma-Aldrich) and irradiated with 20 mW cm^{-2} UV light (365 nm) for 60 s. The plates were kept at 21 °C for 1 h for collagen crosslinking and then moved to 37 °C incubator for 30 min. Each well received 500 µL of T cell media and media was changed daily.

T cell migration was recorded on Day 1 and Day 3 by using an environmentally controlled microscope (Cell Discoverer 7, Zeiss). Here, a 100 µm *Z*-stack with a 50 µm interval was taken in each well ≈100 µm above the glass surface. Images were taken every 3 minutes for 2 h. The images were Z-projected using a script in ImageJ, and cell migration was analyzed using a spot-tracking algorithm in Imaris (Bitplane Inc.). The resulting raw migration data was compiled in MATLAB (MathWorks Inc.) and analyzed in Prism (GraphPad Inc.).

T-Cell-Mediated Killing of Printed B16-F10 Melanoma Filaments: µPOROS collagen matrices were prepared as previously described by compacting sacrificial microparticles within 4 mg mL^{-1} collagen and kept on ice. After compaction and removal of supernatant, either pmel-1 or wild-type $CD8^+$ T cells were mixed into the µPOROS collagen matrix. Here, a 10× concentration of T cells was suspended in 4 mg mL^{-1} collagen and added 1:10 (v/v) to the µPOROS collagen matrix. In this study, the final concentration of T cells was 4 × 10^6 cells per mL of material. For the control B16-F10-only condition, 4 mg mL^{-1} collagen without cells was added 1:10 (v/v) to the µPOROS collagen matrix. To ensure homogeneity, the additional collagen was gently mixed with the µPOROS collagen material using a 1 mL syringe with a 1.6 mm inner-diameter tapered nozzle being sure to avoid introduction of air bubbles into the material. The µPOROS collagen material with or without T cells was then transferred to prechilled custom silicone chambers and kept at 4 °C until printing.

A B16-F10 melanoma cell ink was prepared as previously described by compacting a cell suspension within a 1 mL glass syringe and kept on ice until printing. The syringe was mounted to the 3D printer and the melanoma cell ink was extruded as previously mentioned at a constant volumetric flow rate of 0.1 µL s^{-1}. Following printing, the constructs were placed at 21 °C for 1 h and 37 °C for 30 min. Next, 1 mL of T cell media supplemented with IL-2 was added to each chamber, and cell culture media was changed daily. In the experiments in which B16-F10 and pmel-1 $CD8^+$ T cells were fluorescently labeled to visualize the dynamics between the embedded tumor cells and immune cells, prior to the printing process, B16-F10 cells were stained with 5 µM CellTracker Green CMFDA (ThermoFisher Scientific) and Pmel-1 $CD8^+$ T cells were stained with 5 µM CellTracker Orange CMRA (ThermoFisher Scientific). Time-lapse images were acquired using an inverted confocal microscope with 3 min intervals for a total of 2 h on Day 0 starting at 6 h post printing.

Cell viability assays were performed on Day 3 and Day 6 using an acridine orange/propidium iodide stain. First, samples were washed twice by adding 1 mL of 1× PBS and incubating for 5 min before removal. Acridine orange was prepared at 8.333 µM and propidium iodide was prepared at 1.67 µM in serum-free RPMI base media. Next, 500 µL of the AOPI stain was added to the samples and incubated at 37 °C for 2 h protected from light. After 2 h, the AOPI stain was removed and the samples were washed 3× with 1× PBS at 5 min per wash. The samples were then imaged using an inverted confocal microscope and confocal *Z*-stacks of the tumors were acquired. Cell viability was assessed by analyzing four regions of interest within each biological replicate. An automated ImageJ script was used to threshold the ROI image for each channel, and viability was quantified by measuring area of live signal compared to total signal (Figure S18, Supporting Information).

Immunofluorescence Imaging: Samples were washed twice with PBS and fixed with formalin (Sigma-Aldrich) in PBS for 45 min at room temperature. After fixation, samples were permeabilized with 0.5% Triton X-100 (Sigma-Aldrich) in PBS for 1 h at room temperature. Next, samples were blocked using a blocking buffer comprised of 10% donkey serum (Sigma-Aldrich), 10 µg mL^{-1} Heparin (Sigma-Aldrich), 0.1% Triton X-100, and 0.01% Sodium Azide (Sigma-Aldrich) in PBS overnight at 4 °C. Then, primary antibodies (Ki67 (1:500, ab15580, Abcam)) were added in blocking buffer for 48 h. The primary antibodies were then removed by washing

three times with PBS, and Alexa Fluor-conjugated secondary antibodies were added 1:500 in blocking buffer for 48 h. Secondary antibodies were removed by washing three times with PBS, and nuclei were labeled with DAPI (1:1000, Thermo Scientific) and actin was labeled with ActinRed-555 (Invitrogen) in PBS for 2 h.

Statistical Analysis: Data are presented as mean ± standard deviation (SD) unless otherwise stated. For all analysis unless otherwise stated, *t*-test, or two-way analysis of variance (ANOVA) with Holm-Sidak correction was used. Statistical significance was defined as $p \leq 0.05$. Statistical analysis was performed using GraphPad Prism.

Supporting Information

Supporting Information is available from the Wiley Online Library or from the author.

Acknowledgements

The authors thank S. Uzel for the design and fabrication of a custom syringe extrusion system as well as valuable input, and M. Mata for assistance with cell culture. The authors would also like to thank J. Ahrens, M. Sobral, and K. Wolf for helpful discussions. The authors are grateful to Douglas Richardson and the Harvard Center for Biological Imaging for the help with live cell imaging. The authors also acknowledge the use of BioRender for illustrations. This research was supported by the National Cancer Institute of the National Institutes of Health under award number U01CA214369 and the Blavatnik Accelerator Program at Harvard University.

Conflict of Interest

The authors have filed a patent on this work.

Author Contributions

D.S.R., I.L., M.L.B., Y.L, N.C.J, E.G., J.O., D.J.M, and J.A.L designed research. D.S.R., I.L., M.L.B., Y.L., N.C.J., E.G., J.O., R.M.D., and M.T.D. performed research. D.S.R., I.L., D.J.M., and J.A.L. wrote the manuscript.

Data Availability Statement

The data that support the findings of this study are available from the corresponding author upon reasonable request.

Keywords

cancer, collagen, embedded bioprinting, immunotherapy, microporogens

Received: November 18, 2022
Revised: April 10, 2023
Published online:

[1] M. A. Skylar-Scott, S. G. M. Uzel, L. L. Nam, J. H. Ahrens, R. L. Truby, S. Damaraju, J. A. Lewis, *Sci. Adv.* **2019**, *5*, eaaw2459.
[2] D. B. Kolesky, K. A. Homan, M. A. Skylar-Scott, J. A. Lewis, *Proc. Natl. Acad. Sci. USA* **2016**, *113*, 3179.
[3] D. B. Kolesky, R. L. Truby, A. S Gladman, T. A. Busbee, K. A. Homan, J. A. Lewis, *Adv. Mater.* **2014**, *26*, 3124.
[4] T. Bhattacharjee, S. M. Zehnder, K. G. Rowe, S. Jain, R. M. Nixon, W. G Sawyer, T. E. Angelini, *Sci. Adv.* **2015**, *1*, 1500655.
[5] T. J. Hinton, Q. Jallerat, R. N. Palchesko, J. H. Park, M. S. Grodzicki, H.-J. Shue, M. H. Ramadan, A. R. Hudson, A. W. Feinberg, *Sci. Adv.* **2015**, *1*, e1500758.
[6] A. Lee, A. R. Hudson, D. J. Shiwarski, J. W. Tashman, T. J. Hinton, S. Yerneni, J. M. Bliley, P. G. Campbell, A. W. Feinberg, *Science* **2019**, *365*, 482.
[7] A. C. Daly, M. E. Prendergast, A. J. Hughes, J. A. Burdick, *Cell* **2021**, *184*, 18.
[8] B. M. Holzapfel, F. Wagner, L. Thibaudeau, J.-P. Levesque, D. W. Hutmacher, *Stem Cells* **2015**, *33*, 1696.
[9] L. Gu, D. J. Mooney, *Nat. Rev. Cancer* **2016**, *16*, 56.
[10] R. Ringquist, D. Ghoshal, R. Jain, K. Roy, *Adv. Drug Delivery Rev.* **2021**, *179*, 114003.
[11] P. L. Graney, D. N. Tavakol, A. Chramiec, K. Ronaldson-Bouchard, G. Vunjak-Novakovic, *iScience* **2021**, *24*, 102179.
[12] R. D. Kamm, *APL Bioeng.* **2021**, *5*, 010402.
[13] D. S. Chen, I. Mellman, *Immunity* **2013**, *39*, 1.
[14] J. S. Jeon, S. Bersini, M. Gilardi, G. Dubini, J. L. Charest, M. Moretti, R. D. Kamm, *Proc. Natl. Acad. Sci. USA* **2015**, *112*, 214.
[15] A. Sobrino, D. T. T. Phan, R. Datta, X. Wang, S. J. Hachey, M. Romero-López, E. Gratton, A. P. Lee, S. C. George, C. C. W. Hughes, *Sci. Rep.* **2016**, *6*, 31589.
[16] D. T. T. Phan, X. Wang, B. M. Craver, A. Sobrino, D. Zhao, J. C. Chen, L. Y. N. Lee, S. C. George, A. P. Lee, C. C. W. Hughes, *Lab Chip* **2017**, *17*, 511.
[17] M. B. Chen, J. A. Whisler, J. Fröse, C. Yu, Y. Shin, R. D. Kamm, *Nat. Protoc.* **2017**, *12*, 865.
[18] R. W. Jenkins, A. R. Aref, P. H. Lizotte, E. Ivanova, S. Stinson, C. W. Zhou, M. Bowden, J. Deng, H. Liu, D. Miao, M. X. He, W. Walker, G. Zhang, T. Tian, C. Cheng, Z. Wei, S. Palakurthi, M. Bittinger, H. Vitzthum, J. W. Kim, A. Merlino, M. Quinn, C. Venkataramani, J. A. Kaplan, A. Portell, P. C. Gokhale, B. Phillips, A. Smart, A. Rotem, R. E. Jones, et al., *Cancer Discovery* **2018**, *8*, 196.
[19] A. R. Aref, M. Campisi, E. Ivanova, A. Portell, D. Larios, B. P. Piel, N. Mathur, C. Zhou, R. V. Coakley, A. Bartels, M. Bowden, Z. Herbert, S. Hill, S. Gilhooley, J. Carter, I. Cañadas, T. C. Thai, S. Kitajima, V. Chiono, C. P. Paweletz, D. A. Barbie, R. D. Kamm, R. W. Jenkins, *Lab Chip* **2018**, *18*, 3129.
[20] H.-G. Yi, Y. H. Jeong, Y. Kim, Y.-J. Choi, H. E. Moon, S. H. Park, K. S. Kang, M. Bae, J. Jang, H. Youn, S. H. Paek, D.-W. Cho, *Nat. Biomed. Eng.* **2019**, *3*, 509.
[21] Y. Zhao, R. Yao, L. Ouyang, H. Ding, *Biofabrication* **2014**, *6*, 035001.
[22] L. Neufeld, E. Yeini, N. Reisman, Y. Shtilerman, D. Ben-Shushan, S. Pozzi, A. Madi, G. Tiram, A. Eldar-Boock, S. Ferber, R. Grossman, Z. Ram, R. Satchi-Fainaro, *Sci. Adv.* **2021**, *7*, eabi9119.
[23] O. Chaudhuri, L. Gu, D. Klumpers, M. Darnell, S. A. Bencherif, J. C. Weaver, N. Huebsch, H.-P. Lee, E. Lippens, G. N. Duda, D. J. Mooney, *Nat. Mater.* **2016**, *15*, 326.
[24] O. Chaudhuri, J. Cooper-White, P. A. Janmey, D. J. Mooney, V. B. Shenoy, *Nature* **2020**, *584*, 535.
[25] M. Müller, J. Becher, M. Schnabelrauch, M. Zenobi-Wong, *Biofabrication* **2015**, *7*, 035006.
[26] G.-L. Ying, N. Jiang, S. Maharjan, Y.-X. Yin, R.-R. Chai, X. Cao, J.-Z. Yang, A. K. Miri, S. Hassan, Y. S. Zhang, *Adv. Mater.* **2018**, *30*, 1805460.
[27] G. Ying, N. Jiang, C. Parra-Cantu, G. Tang, J. Zhang, H. Wang, S. Chen, N.-P. Huang, J. Xie, Y. S. Zhang, *Adv. Funct. Mater.* **2020**, *30*, 2003-740.
[28] J. Yin, M. Yan, Y. Wang, J. Fu, H. Suo, *ACS Appl. Mater. Interfaces* **2018**, *10*, 6849.

[29] L. Ouyang, J. P. K. Armstrong, Y. Lin, J. P. Wojciechowski, C. Lee-Reeves, D. Hachim, K. Zhou, J. A. Burdick, M. M. Stevens, *Sci. Adv.* **2020**, *6*, eabc5529.
[30] L. Ouyang, J. P. Wojciechowski, J. Tang, Y. Guo, M. M. Stevens, *Adv. Healthcare Mater.* **2022**, *11*, 2200027.
[31] W. Wu, A. Deconinck, J. A. Lewis, *Adv. Mater.* **2011**, *23*, H178.
[32] A. K. Grosskopf, R. L. Truby, H. Kim, A. Perazzo, J. A. Lewis, H. A. Stone, *ACS Appl. Mater. Interfaces* **2018**, *10*, 23353.
[33] E. Sideris, D. R. Griffin, Y. Ding, S. Li, W. M. Weaver, D. Di Carlo, T. Hsiai, T. Segura, *ACS Biomater. Sci. Eng.* **2016**, *2*, 2034.
[34] J. M. De Rutte, J. Koh, D. Di Carlo, *Adv. Funct. Mater.* **2019**, *29*, 1900071.
[35] C. B. Highley, K. H. Song, A. C. Daly, J. A. Burdick, *Adv. Sci.* **2019**, *6*, 1801076.
[36] L. Riley, L. Schirmer, T. Segura, *Curr. Opin. Biotechnol.* **2019**, *60*, 1.
[37] S. Xin, D. Chimene, J. E. Garza, A. K. Gaharwar, D. L. Alge, *Biomater. Sci.* **2019**, *7*, 1179.
[38] T. G. Molley, G. K. Jalandhra, S. R. Nemec, A. S. Tiffany, A. Patkunarajah, K. Poole, B. A. C. Harley, T.-T. Hung, K. A. Kilian, *Biomater. Sci.* **2021**, *9*, 4496.
[39] V. G. Muir, T. H. Qazi, J. Shan, J. Groll, J. A. Burdick, *ACS Biomater. Sci. Eng.* **2021**, *7*, 4269.
[40] T. H. Qazi, J. Wu, V. G. Muir, S. Weintraub, S. E. Gullbrand, D. Lee, D. Issadore, J. A. Burdick, *Adv. Mater.* **2022**, *34*, 2109-194.
[41] T. Bhattacharjee, C. J. Gil, S. L. Marshall, J. M. Urueña, C. S. O'bryan, M. Carstens, B. Keselowsky, G. D. Palmer, S. Ghivizzani, C. P Gibbs, W. G Sawyer, T. E. Angelini, *ACS Biomater. Sci. Eng.* **2016**, *2*, 1787.
[42] T. Bhattacharjee, T. E. Angelini, *J. Phys. D: Appl. Phys.* **2019**, *52*, 024006.
[43] C. D. Morley, C. T. Flores, J. A. Drake, G. L. Moore, D A. Mitchell, T. E. Angelini, *Int. J. Bioprint.* **2022**, *28*, 00231.
[44] J. A. Brassard, M. Nikolaev, T. Hübscher, M. Hofer, M P. Lutolf, *Nat. Mater.* **2021**, *20*, 22.
[45] B. S. Kim, W.-W. Cho, G. Gao, M. Ahn, J. Kim, D.-W. Cho, *Small Methods* **2021**, *5*, 2100072.
[46] M. G. Patino, M. E. Neiders, S. Andreana, B. Noble, R E. Cohen, *Implant Dent.* **2002**, *11*, 280.
[47] M. J. Paszek, N. Zahir, K. R. Johnson, J. N. Lakins, G. I. Rozenberg, A. Gefen, C. A. Reinhart-King, S. S. Margulies, M. Dembo, D. Boettiger, D. A. Hammer, V. M. Weaver, *Cancer Cell* **2005**, *8*, 241.
[48] K. R. Levental, H. Yu, L. Kass, J. N. Lakins, M. Egeblad, J. T. Erler, S. F. T. Fong, K. Csiszar, A. Giaccia, W. Weninger, M. Yamauchi, D. L. Gasser, V. M. Weaver, *Cell* **2009**, *139*, 891.
[49] F. Spill, D. S. Reynolds, R. D. Kamm, M. H. Zaman, *Curr. Opin. Biotechnol.* **2016**, *40*, 41.
[50] J. Stepanovska, M. Supova, K. Hanzalek, A. Broz, R. Matejka, *Biomedicines* **2021**, *9*, 1137.
[51] H. Lyng, O. Haraldseth, E. K. Rofstad, *Magn. Reson. Med.* **2000**, *43*, 828.
[52] U. Del Monte, *Cell Cycle* **2009**, *8*, 505.
[53] A. Ladányi, J. Kiss, B. Somlai, K. Gilde, Z. Fejős, A. Mohos, I. Gaudi, J. Tímár, *Cancer Immunol. Immunother.* **2007**, *56*, 1459.
[54] K. Wolf, M. Te Lindert, M. Krause, S. Alexander, J. Te Riet, A. L. Willis, R. M. Hoffman, C. G. Figdor, S. J. Weiss, P. Friedl, *J. Cell Biol.* **2013**, *201*, 1069.
[55] J. D. Abad, C. Wrzensinski, W. Overwijk, M. A. De Witte, A. Jorritsma, C. Hsu, L. Gattinoni, C. J. Cohen, C. M. Paulos, D. C. Palmer, J. B. A. G. Haanen, T. N. M. Schumacher, S. A. Rosenberg, N. P. Restifo, R. A. Morgan, *J. Immunother.* **2008**, *31*, 1.
[56] S. Spranger, D. Dai, B. Horton, T. F. Gajewski, *Cancer Cell* **2017**, *31*, 711.
[57] A. Boissonnas, L. Fetler, I. S. Zeelenberg, S. Hugues, S. Amigorena, *J. Exp. Med.* **2007**, *204*, 345.
[58] M. Mulazzani, S. P. Fräßle, I. Von Mücke-Heim, S. Langer, X. Zhou, H. Ishikawa-Ankerhold, J. Leube, W. Zhang, S. Dötsch, M. Svec, M. Rudelius, M. Dreyling, M. Von Bergwelt-Baildon, A. Straube, V. R. Buchholz, D. H. Busch, L. Von Baumgarten, *Proc. Natl. Acad. Sci. USA* **2019**, *116*, 24275.
[59] T. Honda, J. G. Egen, T. Lämmermann, W. Kastenmüller, P. Torabi-Parizi, R. N. Germain, *Immunity* **2014**, *40*, 235.
[60] J. Fu, A. Yu, J. Tang, B. He, W. Chen, *Am. J. Transl. Res.* **2020**, *12*, 7262.
[61] N. Nelson, M. Lopez-Pelaez, A. Palazon, E. Poon, M. De La Roche, S. Barry, V. Valge-Archer, R. W. Wilkinson, S. J. Dovedi, P. D. Smith, *Oncoimmunology* **2019**, *8*, 1.
[62] F. Hofmann, M. Navarrete, J. Álvarez, I. Guerrero, M. A. Gleisner, A. Tittarelli, F. Salazar-Onfray, *Int. J. Mol. Sci.* **2019**, *20*, 4509.
[63] S. M. Amos, H J. Pegram, J. A. Westwood, L. B. John, C. Devaud, C. J. Clarke, N. P. Restifo, M. J. Smyth, P. K. Darcy, M. H. Kershaw, *Cancer Immunol. Immunother.* **2011**, *60*, 671.
[64] D. S. Reynolds, K. M. Tevis, W. A. Blessing, Y. L. Colson, M. H. Zaman, M. W. Grinstaff, *Sci. Rep.* **2017**, *7*, 10382.
[65] K. M. Charoen, B. Fallica, Y. L. Colson, M. H. Zaman, M. W. Grinstaff, *Biomaterials* **2014**, *35*, 2264.
[66] D. S. Reynolds, K. M. Bougher, J. H. Letendre, S. F. Fitzgerald, U. O. Gisladottir, M. W. Grinstaff, M. H. Zaman, *Acta Biomater.* **2018**, *77*, 85.
[67] W. J. Polacheck, M. L. Kutys, J. B. Tefft, C. S. Chen, *Nat. Protoc.* **2019**, *14*, 1425.